

Interferometric calibration and the first elevation observations at EKB ISTP SB RAS radar at 10-12 MHz

Oleg I.Berngardt

Lermontova Str., 126A, Irkutsk, Russia, ISTP SB RAS

Roman R.Fedorov

Lermontova Str., 126A, Irkutsk, Russia, ISTP SB RAS

Pavlo Ponomarenko

Physics building, 116 Science Place, Saskatoon, SK, S7N 5E2, Canada, University of Saskatchewan

Konstantine V.Grkovich

Lermontova Str., 126A, Irkutsk, Russia, ISTP SB RAS

Abstract

The method for calibrating elevation measurements at EKB ISTP SB RAS radar obtained for the period 20/09/2019 - 18/11/2019 is presented. The calibration method is a modernization of the method for calibrating radar by meteor trails. The main difference of the method is the use of not a statistically processed FittACF data, but the full waveform of the signals scattered on the meteor trails. Using the full waveform makes it possible to more reliably distinguish meteor scattering from other possible scattered signal sources, and to determine meteor heights from the trail lifetime using the NRLMSIS-00 model. A comparison of the results with the results of E-layer calibration method shows a good agreement. The first examples of regular elevation observations at the EKB ISTP SB RAS radar are presented, and their preliminary interpretation is given.

Keywords: meteor trails scattering, decameter radars, calibration techniques,

Email addresses: berng@iszf.irk.ru (Oleg I.Berngardt), fedrr@iszf.irk.ru (Roman R.Fedorov), pbp672@usask.ca (Pavlo Ponomarenko), grkovich@iszf.irk.ru (Konstantine V.Grkovich)

1. Introduction

The coherent decameter radars of Super Dual Auroral Network (Super-DARN) (Greenwald et al., 1995; Chisham et al., 2007; Nishitani et al., 2019) and similar radars (Berngardt et al., 2015b) are effective instruments for studying the magnetosphere-ionosphere interaction and for the upper atmosphere monitoring by radiowave scattering technique. Radars are the instruments with the regular spatial resolution 15-45km, the regular temporal resolution 1-2 minutes, the maximum range 3500-4500km, and nearly 50° field-of-view in azimuth.

The decameter radars operate at 8-20 MHz, so ionospheric refraction plays a significant role. The sources of the scattered signals received by the radars are: the meteor trail scattering in D- and E- layers of the ionosphere (Yukimatu and Tsutsumi, 2002), scattering from E- and F-layer ionospheric irregularities elongated with the Earth magnetic field (Greenwald et al., 1995; Chisham et al., 2007), signals scattered by surface (ground and water) irregularities and detected due to refraction of radiowaves in the ionosphere (Ponomarenko et al., 2010; Greenwood et al., 2011), mesospheric echoes (Hosokawa et al., 2004, 2005; Ogunjobi et al., 2015) and other possible mechanisms (Ponomarenko et al., 2016). The propagation trajectory of the radio wave affects both the accuracy of identifying the scattered signal type (Bland et al., 2014) and the accuracy of determining the parameters of ionospheric irregularities: their velocity (Ponomarenko et al., 2009; Gillies et al., 2011), altitude (Koustov et al., 2007; Ponomarenko et al., 2009) and geographical coordinates (Villain et al., 1984; Ponomarenko et al., 2009; Berngardt et al., 2015a). Therefore, the trajectory estimation is a complex theoretical and computational problem and is the basis for solving important practical problems of using decameter coherent radars for ionospheric and magnetospheric monitoring.

One of the main methods to improve the accuracy of the radiowave propagation trajectory estimate are elevation (vertical angle of arrival, interferometric)

observations (Villain et al., 1984). Due to the relatively long wavelength, comparable with the distance from the antenna to the ground surface, the thermal variations in radio cables and the analog parts of the transmitter and receiver parts, the elevation observations require a regular phase calibration (Chisham and Freeman, 2013; Chisham, 2018; Ponomarenko et al., 2018). Due to the potential dynamics of the calibration parameters, such a technique should be automatic.

The main problem with calibration of SuperDARN interferometry is that for direct calibration using a fixed source at a given location one needs to put a target at about 100 km altitude and about 300-500 km range due to the scale of measurements. It is practically impossible and other techniques are used. Currently at SuperDARN radars the following basic calibration methods are used: by using the position of the ground scatter signal (Ponomarenko et al., 2015); by using the signals scattered in the E-layer of the ionosphere (Ponomarenko et al., 2018); by using the signals scattered by the meteor trails (Chisham and Freeman, 2013; Chisham, 2018); and by using the ionospheric targets with known geographic location, for example heater-induced artificial irregularities (Burrell et al., 2016).

Ground scatter calibration is based on adjusting the phase difference between the main and interferometer antenna arrays in such a way that the resulting elevation approaches the theoretically expected zero values at the far edge of the ground scatter band for any given 'hop' (Ponomarenko et al., 2015). The main problem of the method is the intrinsically high dynamics in the ground scatter range distribution due to strong variability of the ionospheric parameters, which requires visual analysis of the data and effectively prohibits automatic calibration process.

Less affected by the ionospheric refraction and therefore more suitable for automatic processing are the methods based on using scattering in E- and D-layers - the lower part of the ionosphere.

In the case of using the signals scattered in the E-layer of the ionosphere, the calibration procedure is based on matching the observed phase distribution from

the farthest ranges of the E-layer echoes, where the elevation angle is expected to be nearly zero, with the simulated distribution produced by using a simple statistical model of the E-layer backscatter returns (Ponomarenko et al., 2018). Using this approach allows one to improve the accuracy of calibration in comparison with that in (Ponomarenko et al., 2015) due to much lower variability in the E-layer altitude as compared to that of the F-layer. Furthermore, this approach does not require taking into account a refraction in the ionosphere which allows creating an automatic calibration algorithm. In this case, the calibration is performed over the data produced by standard SuperDARN programs: the phase of the correlation function between the signals received at main and interferometric antenna arrays and averaged over the number of soundings. Another technique presented in (Chisham and Freeman, 2013; Chisham, 2018) allows calibrating measurements by adjusting the phase offset in such a way that the effective altitude of scattering at meteor trails (D- and E-layers) is the same across several range gates.

The problem of the both methods is the complexity of independent measurement of the height of the scattering irregularity, found either by optimization of the residual functional (Chisham, 2018), by measuring average spectral widths (Chisham and Freeman, 2013), or by substituting a model height (Ponomarenko et al., 2018). Another problem of these methods is detecting scattered signals of necessary kind and differing them from other signals, because misidentification leads to processing errors. Using large amount of sounding data, however, can mitigate these problems (Chisham, 2018; Ponomarenko et al., 2018).

In this paper, we present a method for calibrating the elevation measurements at EKB ISTP SB RAS radar by using the signals scattered on meteor trails, improving (Chisham and Freeman, 2013; Chisham, 2018) technique. The problems of determining the scattering height and detecting the scattering type are solved by independent algorithms. They are based on the physical mechanisms of the meteor echo formation and on the automatic analysis of the received signals quadrature components.

2. Calibration method

The EKB ISTP SB RAS (Berngardt et al., 2015b) is mid-latitude coherent radar installed in 2012 by the Institute of Solar-Terrestrial Physics, Siberian Branch of the Russian Academy of Sciences (ISTP SB RAS) in the Arti Observatory of Institute of Geophysics, Ural Branch of the Russian Academy of Sciences ($56.43^{\circ}N$, $58.56^{\circ}E$, Sverdlovsk Region, Russia, 180 km south-west from Ekaterinburg). The radar electronics was produced for ISTP by University of Leicester (UK) and is an analogue of the SuperDARN CUTLASS stereo radar (Lester et al., 2004). The radar operates at 8-20MHz and uses standard SuperDARN radar software to process sounding data. The antenna pattern of the radar is formed by 20 DLP11 (Titanex GmbH, Germany) log-periodic antennas located in two linear equidistant phased arrays: transmit-receive one (16 antennas, main array) and receive one (4 antennas, interferometric array). This construction of the radar allows one to scan the 52° radar field-of-view in 16 fixed directions (beams). The radar field of view and beam positions are shown in Fig.1A. The azimuthal resolution of the radar is $3 - 6^{\circ}$, depending on the frequency. For elevation angle observations the combination of main and interferometric arrays is used. The antenna field geometry is shown in Fig.1B. The signals received from each antenna in the phased array are summarized with necessary phase differences for the radar beam forming. The DLP11 antenna pattern is quite complex, frequency dependent and has the significant back lobe. The model calculations of the antenna pattern using MMANA-GAL software (MMANA-GAL software) are shown in Fig.1C-D. Such an antenna pattern leads to a noticeable number of the signals received in the back lobe of the antenna pattern and should be taken into account when processing the data.

The measurements of the phase difference between the signals received by main and interferometric antenna arrays provide the elevation angles estimations and require calibration. Due to the linear orientation of the main and interferometric arrays, the antenna pattern at a fixed azimuth for each of the arrays corresponds to the surface of a cone (Fig.1E), and the azimuth should

be taken into account when calculating elevation. The $2\pi n$ uncertainty in the calculation of the phase caused by the large distance between main and interferometric arrays should be taken into account too.

To calibrate elevation observations we choose the meteor calibration method (Chisham and Freeman, 2013; Chisham, 2018), modified to use wide capabilities of the EKB ISTP SB RAS radar to process meteor trail scattering. The calibration method (Chisham, 2018) uses processed data, extracts meteor signals by range ($<400\text{km}$) and determines the average meteor trail height using algorithmic optimization. In (Chisham and Freeman, 2013) the meteor trail height is determined from average spectral width.

Our method uses exclusively the waveform of signals scattered from meteor trails measured on two phased arrays. The scattering height is calculated based on the shape of the scattered signal using the reference model of the neutral atmosphere NRLMSIS-00 (Picone et al., 2002).

There are two types of scattering on meteor trails, differing by the ratio of the trail plasma frequency to the sounding frequency: underdense and overdense echo.

To calibrate the elevation observations we use underdense echo because their cross-section exponentially decrease with time and they are easy to detect. Their dynamics is controlled by recombination processes and in the first approximation is related to the diffusion coefficient at the burn height (Jones and Jones, 1990) so their altitude can also be detected from the radar data. At EKB radar we use the algorithm for detecting underdense meteor trail echoes, similar to the detection algorithms at specialized meteor radars and SuperDARN radars (Tsutsumi et al., 1999, 2009) but adjusted to use EKB radar features.

Search and selection of meteor trail scattering at EKB radar is carried out using the following scheme:

1. Search for bursts of signal level spatially localized by range and azimuth;

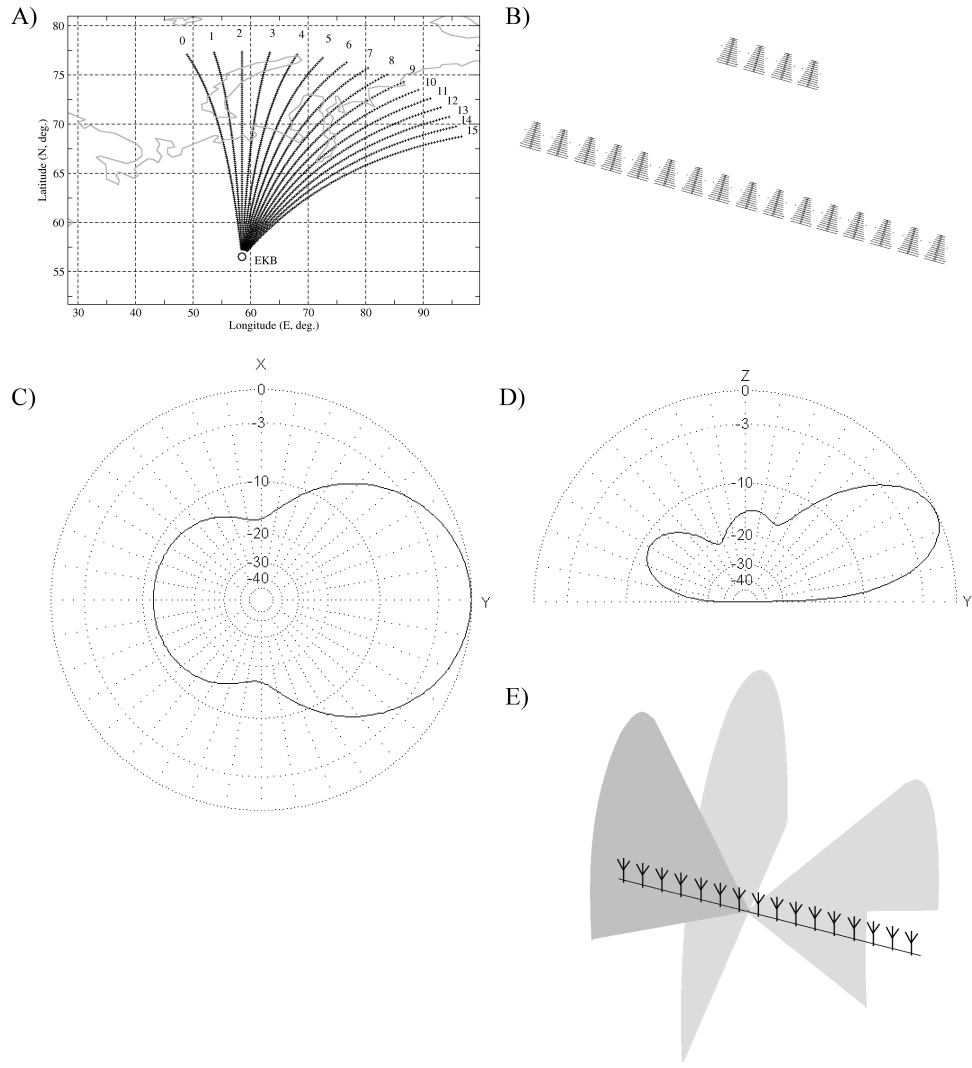


Figure 1: A) EKB ISTB SB RAS radar location and field of view; B) Antenna field geometry; C-D) DLP11 antenna pattern at 10MHz in the horizontal and vertical plane correspondingly (model calculations). E) Antenna pattern cone for 3 different azimuths;

2. Fit separately the amplitude and the phase of the signal by the model

$$\begin{cases} A_m(t) = \theta(t)A_0e^{-\frac{t}{\tau}} \\ \phi_m(t) = \theta(t)(st + \phi_0) \end{cases} \quad (1)$$

where $A_m(t)$ is the model amplitude; $\phi_m(t)$ is the model phase; A_0 and ϕ_0 are the initial amplitude and phase; s is linear phase change coefficient proportional to the Doppler drift velocity, τ is characteristic trail lifetime.

3. In the case of high fitting accuracy, interpret the signal as meteor trail scattering with corresponding lifetime and velocity. The fitting accuracy is determined by the variance of the amplitude and phase of the received signal relative to their model values (1).

In this paper we use the characteristic lifetime, associated with the diffusion coefficient at the burning height. The trail lifetime distribution is shown in Fig.2B. Using the neutral atmosphere model and trail lifetime makes it possible to determine the coordinates of the scattering point without using elevation observations.

The characteristic meteor trail lifetime τ of the underdense echo is defined by the diffusion coefficient D at the burn height (Tsutsumi et al., 2009; Chisham and Freeman, 2013):

$$\tau = \frac{\lambda^2}{32\pi^2 D} \quad (2)$$

and the diffusion coefficient is:

$$D = \frac{6.39 * 10^{-2}KT^2}{p} \quad (3)$$

where λ is sounding signal wavelength; T is absolute temperature; p is the pressure; K is the mobility coefficient of the ions in the meteor trail, usually taken as $2.2 \cdot 10^{-4}m^2s^{-1}V^{-1}$ (Tsutsumi et al., 2009).

The burn height is determined by the NRLMSIS-00 model (NRLMSISE-00) for a given time and coordinates, by iterative search over the heights. The distribution of the burn heights calculated according to the EKB radar data

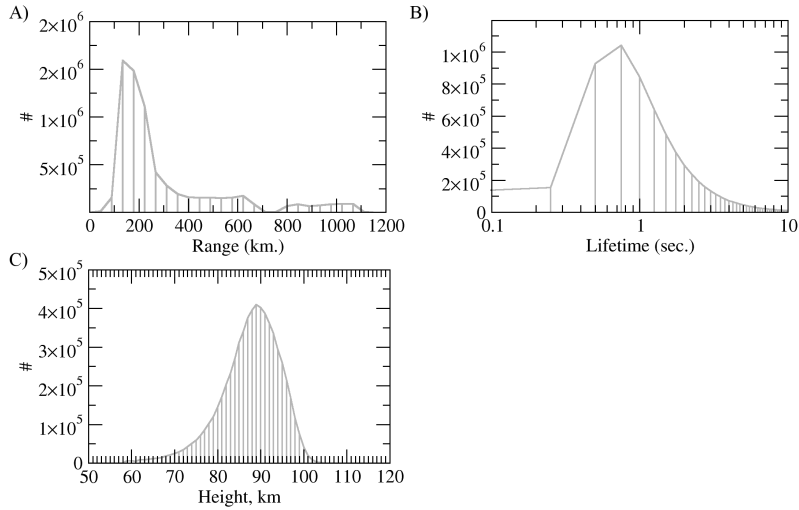


Figure 2: Distributions of meteors (histograms) observed on the EKB radar during 2017-2019 by ranges (A), lifetimes (B) and burn heights (C).

over the period 2017-2019 is shown in Fig.2C. As can be seen from the figure, the main part of the distribution corresponds to heights 80-100 km with the most probable burn height 89 km, which is in a good agreement with the results obtained earlier (Holdsworth et al., 2004).

Refraction at altitudes lower than the meteor's burn altitudes is weak and the sounding signal trajectory is linear. Using this approach the interferometer can be calibrated using the radar observations only.

Fig.3A-D shows examples of signals scattered on meteor trails and received by the two arrays of the radar the main (black line) and intererometric (gray line), obtained with a high correlation coefficient ($R > 0.8$). The figure demonstrates a good correlation between the shapes of the real (left) and imaginary (right) components of the received signal. A high degree of correlation of the shapes of the received signal, its long lifetime (of the order of 0.3-0.5 seconds) and its complex shape allow to detect meteors and stably measure the phase difference between signals received by the two antenna arrays with a good accuracy.

Fig.4A shows the distribution of the correlation coefficients between signals received by different arrays. It can be seen from the figure that the most probable value of the correlation coefficient is 0.76, and the number of observations with a correlation coefficient >0.8 is about 15%. The high average number of observed meteors (>200 per hour) and the large number of meteor trail signals observed by both arrays allow using a large number of meteor observations for EKB radar calibration. For the calibration, we select only meteor data during the period 20/09/2019-18/11/2019 observed by both phased arrays at ranges above 250km and below 750km with a high correlation coefficient ($R>0.8$). The restriction of ranges below 250km is used to reduce the influence of spatial resolution to the accuracy of determining the elevation angle and thereby to increase the accuracy of calibrated elevation data. The upper limit 750km is used for additional decrease of the number of possible ground scatter signals and signals scattered by ionospheric irregularities on the resulting observation statistics. The lower limit of the correlation coefficient is used to increase the accuracy of determining the interference phase of the received signals.

The total number of meteor trails used for calibration is about 1500. The distributions of the meteor trails over the heights and the ranges are shown in Fig.4B-C correspondingly.

To calibrate the phase difference between the phased arrays, the model and experimental phases have been compared. The experimental phase difference was determined as the phase providing maximal cross-correlation coefficient between the signals received by both arrays.

The model phase difference is obtained from geometric considerations as the following:

$$\begin{aligned} \Delta\varphi_{mod,i} &\approx 2\pi \frac{\Delta_y \cos(\theta_i)}{\lambda_{0,i}} \cos\left(\alpha_i - \text{atan}\left(\frac{\Delta_z}{\Delta_y \cos(\theta_i)}\right)\right) \\ \alpha_i &= \text{asin}\left\{\frac{(R_E + H_i)^2 - (R_E^2 + R_i^2)}{2R_E R_i}\right\} \end{aligned} \quad (4)$$

where Δ_y, Δ_z are the displacement of the center of the interference array relative to the center of the main array in the horizontal and vertical directions

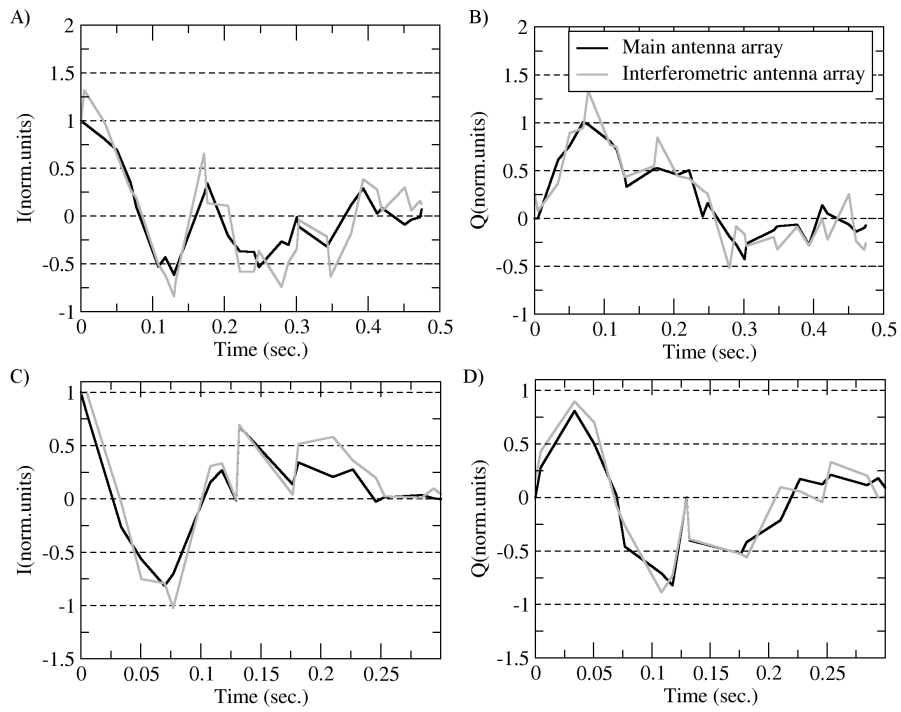


Figure 3: Examples of meteor echoes recorded by different arrays - the black line corresponds to the main array, the green - to the interferometric array. On the left are the I-components of the received signals, on the right are the Q-components. The amplitudes are normalized.

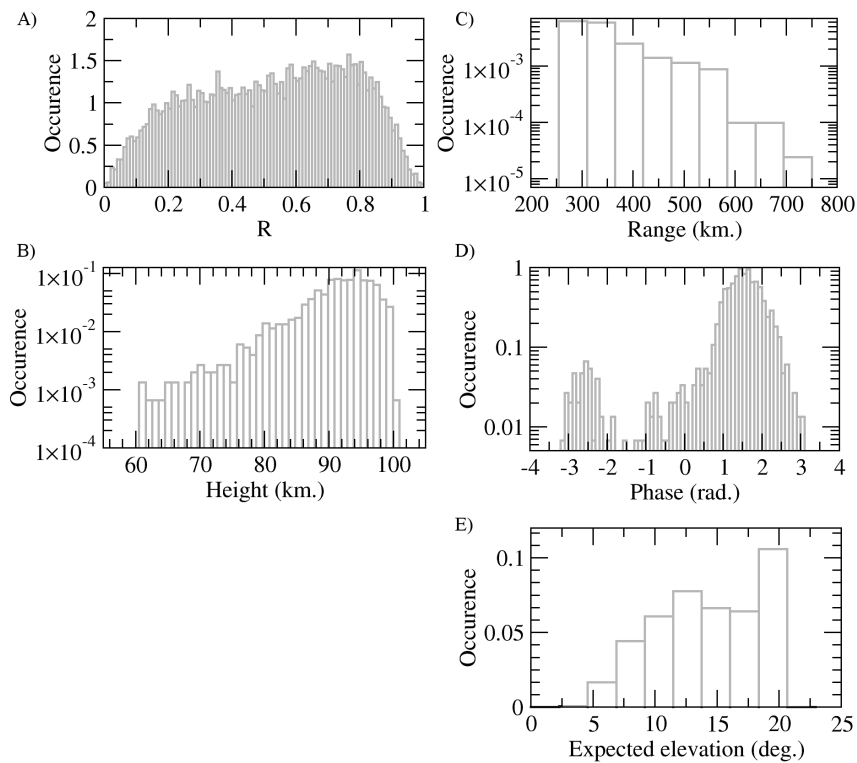


Figure 4: Statistical distributions of the meteor trail characteristics used for the calibration. A) is the distribution of the meteor correlation coefficients between the antenna arrays; B) is the distribution of filtered (250-750km, $R > 0.8$) meteors over altitude; C) is the distribution of filtered (250-750km, $R > 0.8$) meteors over the ranges; D) is the distribution of filtered (250-750km, $R > 0.8$) meteors over the estimated phase difference; E) is the distribution of filtered (250-750km, $R > 0.8$) meteors over the expected elevation angles.

correspondingly (56.4 and -3.8 meters); H_i, R_i - are the height of the observation of the i -th meteor trail and the distance to it, correspondingly; $\lambda_{0,i}, \theta_i$ are the wavelength of the sounding signal and the ground azimuth to the meteor trail relative to the center of the radar field-of-view, correspondingly; R_E is the radius of the Earth; α_i is the estimated elevation angle of the observed meteor trail.

It is traditionally supposed that the phase discrepancy between model and experimental phase observations is associated with a total phase shift between the receivers and the difference in the electric propagation lengths of the signal from the phased arrays to the receivers (Chisham, 2018; Ponomarenko et al., 2018). As a preliminary analysis showed, the EKB has a significant non-linear component of the phase difference caused by the hardware. Therefore, the calibration problem in this paper was solved for the basic operating frequencies of the radar 10-12MHz only. This allows us to neglect the frequency dependence of the phase difference and reduce the calibration problem to the search for a single unknown parameter A . The parameter should minimize the difference between the model phase difference $\Delta\varphi_{mod,i}$ and the experimental phase difference $\Delta\varphi_{exp,i}$ for all meteor trails:

$$\sum_{i=1}^N [\Delta\varphi_{exp,i} - (\Delta\varphi_{mod,i} + A)]^2 = 0 \quad (5)$$

here the summation is made over all the N detected meteor trails.

The distributions of the expected antenna phase difference and elevations of the observed meteors are shown in Fig.4D-E. It can be seen from Fig.4D that about 4% of meteor tails are observed in the back lobe of the antenna pattern (which corresponds to phases <-2 radians), which should be taken into account in the calibration algorithm. A small part of such trails allows us simply to remove them from consideration, and this should not significantly affect the accuracy of the resulting algorithm. The final algorithm for determining the calibration coefficient A becomes a three-stage one:

1. based on the data set that simultaneously satisfies the conditions $R >$

- 0.8, $R_i > 250km$, $R_i < 750km$, the first approximation of the calibration coefficient A_0 is made using (5);
2. the observations in the back lobe of the antenna pattern are removed. They are defined as observations that differ from the dependence found at the first stage by more than 1 radian: $|\Delta\varphi_{exp,i} - (\Delta\varphi_{mod,i} + A_0)| > 1$;
 3. based on the remaining data set, more accurate calibration coefficient A is found using (5).

It should be noted that in contrast to the methods (Chisham, 2018; Ponomarenko et al., 2018), the main parameter used for calibration is not a statistical dependence of the phase characteristics on the radar range, but the difference between the expected and observed phase for each meteor trail. In contrast to (Chisham and Freeman, 2013) the shape of the signal scattered by meteor trail is used for calibration, but not its average parameters produced by FitACF algorithm.

For the calibration, we processed about 2 months of interferometric observations at the EKB radar - from 20/09/2019 to 18/11/2019. This results the calibration coefficient $A = -0.58$ radian. It differs slightly from the first approximation $A_0 = -0.49$ radian. This can be explained by the small number of observations in the back lobe of the antenna pattern. The resulting distributions of the expected phase and the calibrated experimentally observed phase for different beams are shown in Fig.5. It can be seen from the figure that the calibration satisfactorily describes the experimental data on all the beams (the expected linear dependence is shown by the black line). Variations of the observed phase near the expected value can be associated both with a significant dependence of the phase difference on the azimuth (caused by the hardware used for the formation of the antenna pattern) and with a significant level of the noise during the observations - both auxiliary noise (Berngardt et al., 2018) and the noise of the analog receivers.

The obtained results have been validated using technique (Ponomarenko et al., 2018) which estimates time delay δT between main and interferometric

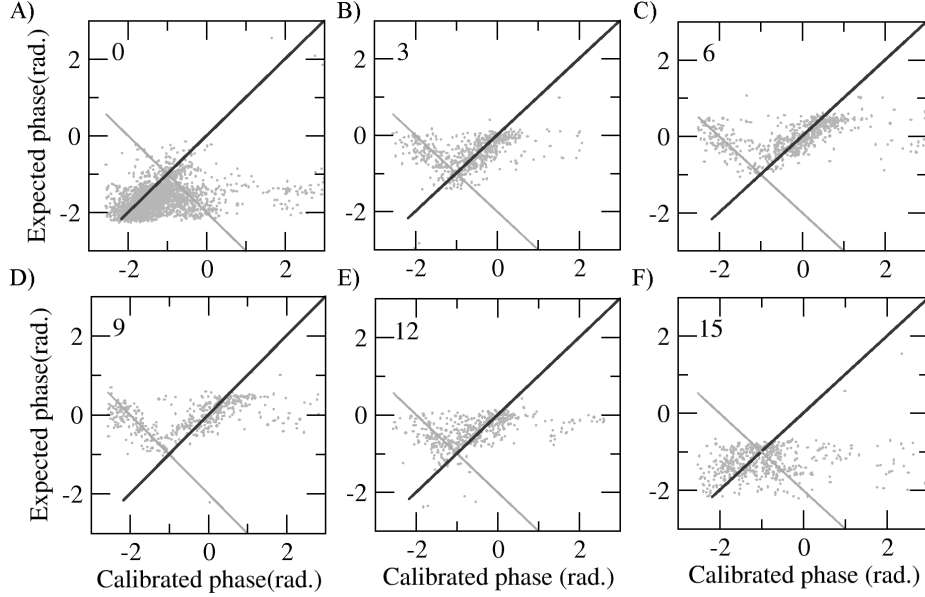


Figure 5: Distribution of calibrated phases for signals scattered by meteor trails. Black line corresponds to the main lobe scattering, gray line - to the back lobe scattering.

channel. The calibration coefficient A in this case becomes

$$A = 2\pi f_0 \delta T \quad (6)$$

This technique requires a statistically significant amount of E-layer echoes, so we applied to the data from 28/09/2019 when the E-layer scatter was clearly observed (see Fig.6). Our analysis produced the estimate of $\delta T = -8.4ns$. For standard frequency used in this experiment 11.2MHz this corresponds to the calibration coefficient $A \approx -0.591$ in very good agreement with the technique presented in this paper.

3. Testing the calibration results using FitACF data

All the previous operations were carried out directly with the quadrature components of the signal. However, when interpreting the experimental data, a two-stage scheme for obtaining processed data is used: at the first (RawACF)

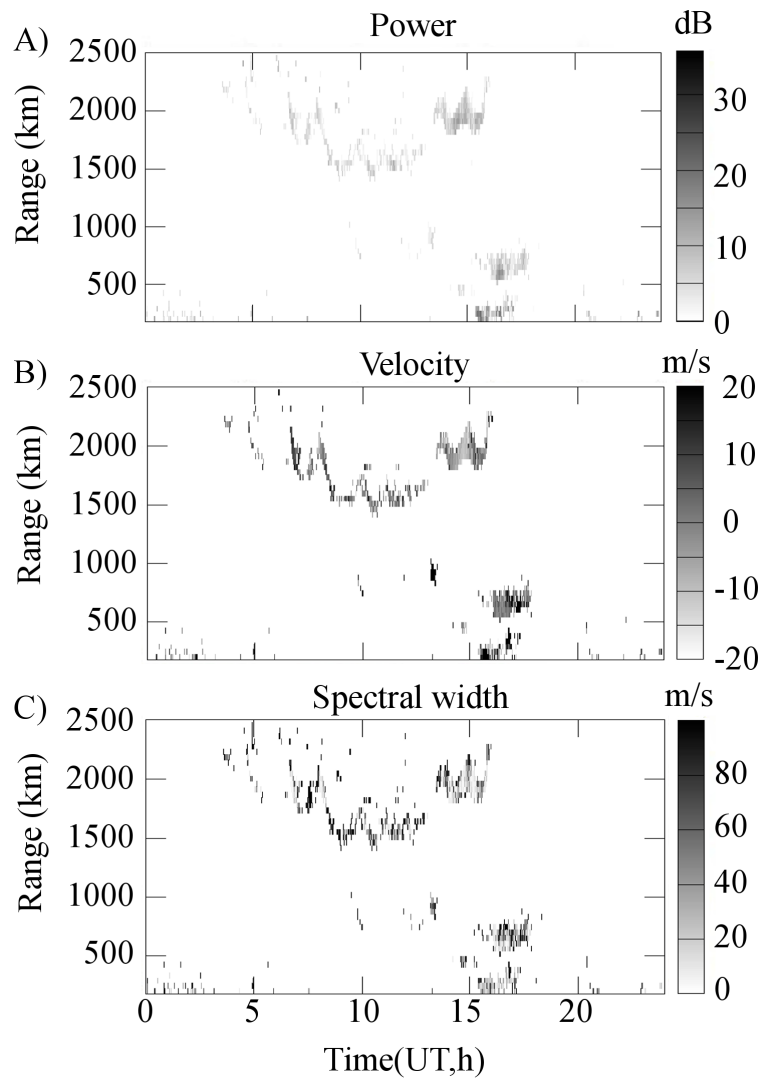


Figure 6: Observed power(A), drift velocity(B) and spectral width(C) during 28/09/2019.

stage, the values of the autocorrelation and cross-correlation functions are obtained (calculated respectively from the main array signals and jointly from the main and interference arrays signals), and at the second (FitACF) stage these correlation functions are used to estimate the parameters of ionospheric irregularities using FitACF algorithm (Ribeiro et al., 2013). The calculation of the difference in interferometric phases and the calculation of the elevation angle is made at the second stage.

Let us demonstrate the effectiveness of the calibration correction obtained by this method for correcting the FitACF data. We studied the measured interference phase obtained at the FitACF stage and calibrated using calculated A . To do this we have processed the complete set of interferometric observational data 20/09/2019 - 18/11/2019 at ranges $<750\text{km}$. For calibration we increase the interference phase from FitACF data by calibration coefficient A obtained in previous analysis and compare them with expected phase for meteor trail scattering. The comparison results are shown in Fig.7. It can be seen from the figure that the received signals contain both the signals scattered by the meteor trails from the main lobe of the antenna pattern (thick line) and the signals from the back lobe (thin line). The figure corresponds well to Fig.4D and Fig.5 - a few percent of the detected signals comes from the back lobe. In the bottom right corner of Fig.7 there are also some signals of not meteoric nature - possibly E-layer scatter or near-range scatter.

To demonstrate the effectiveness of the method to calculate elevation angles, we processed the same observational data during 20/09/2019-18/11/2019 at all the available radar ranges. The elevation angle was calculated from the interference phase difference with taking into account the uncertainty of $2\pi n$, as a minimum value in the range $0^\circ - 45^\circ$ for $n \in [-5, 5]$. A comparison between the calibrated average elevation angle of the received signals and model elevation angle for meteor observations calculated from geometric considerations for a scattering height of 90km is shown in Fig.8A (in the two cases - for plane-layered ionosphere model and for spherical ionosphere model). In the figure we used a plane-layered ionosphere for a model elevation angle, that overestimates

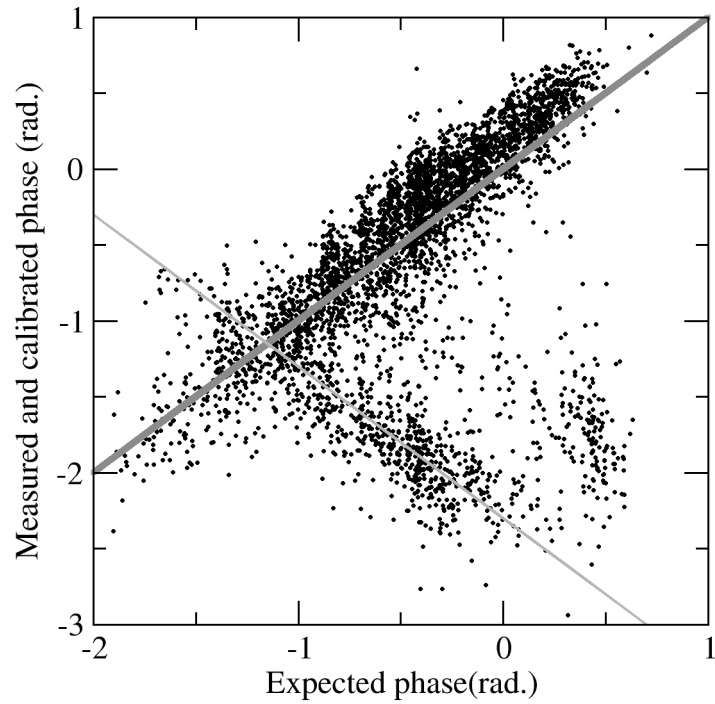


Figure 7: Distribution of the expected phase for meteor trail scattering (calculated from the measured range and standard height 90km) and the measured calibrated phase for September-November 2019 obtained from processed data (FitACF) over the ranges 250-750km. The thick line corresponds to the scattering by meteors in the main lobe of the antenna pattern, the thin line corresponds to the scattering in the back lobe of the antenna pattern.

the expected elevation angle, but gives a positive elevation angle for each range. Fig.8A shows a good agreement between the average measured elevation angles and model ones at the ranges less than 450 km, which confirms well the statement of (Chisham, 2018) about predominant scattering from meteor trails at ranges less than 400 km.

The ratio of the measured elevation angle α_{exp} to the model angle α_{mod} for 90 km scattering allows one to estimate the type of scattering under no refraction assumption, using effective scattering height h_{eff} :

$$h_{eff} = \frac{\alpha_{exp}}{\alpha_{mod}} \cdot 90km \quad (7)$$

The mean effective scattering height is shown in Fig.8. The effective heights above 300 km (taking into account the errors of the plane-layered model) corresponds to a hop signal propagation, therefore, in this experiment, at distances above 900 km the first hop ground scatter is most likely observed. Approximately from the 2300km range (corresponding the effective heights above 900 km), a second hop ground scatter is most likely observed. The intermediate regions most likely correspond to scattering by the ionospheric irregularities of the E- and F- layers.

Fig.9 shows examples of calculated elevation in various experiments and an approximate identification of the scattered signal types depending on the elevation angle and range. Fig.9A shows an example of ionospheric scatter in the F region moving from high to low latitudes. Fig.9B shows an example of simultaneous observation of ionospheric scatter in the E region and scattering at near-range distances, related, judging by a very high elevation angle (> 40 degrees), with possible reflections from sporadic layers. Fig.9C illustrates the case of observing ground scatter signals simultaneously in the main and back lobes of the antenna pattern. Fig.9D shows an example of possible scattering in the E-region.

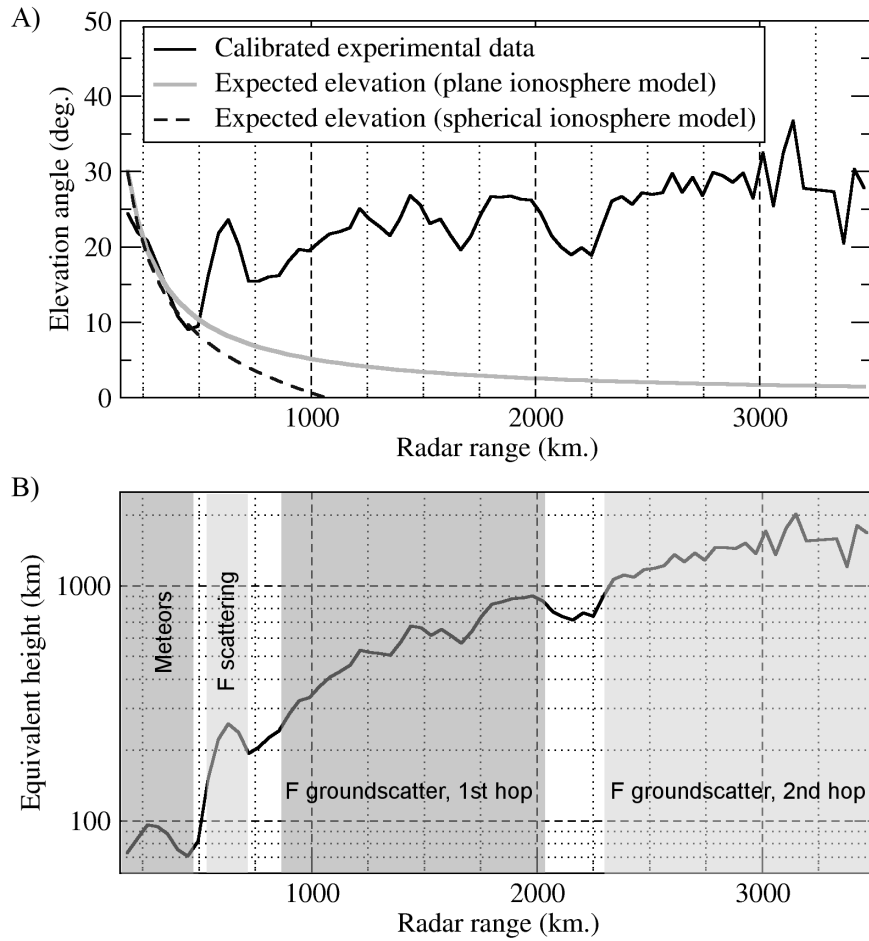


Figure 8: Elevation angle statistics over September-November 2019 (black line), the expected elevation angle in the plane ionosphere model (gray solid line) and in the spherical ionospheric model (black dashed line) (A) and the effective scattering height in the approximation of the linear radiowave propagation calculated from these data (B) in the approximation of a plane-layered ionosphere.

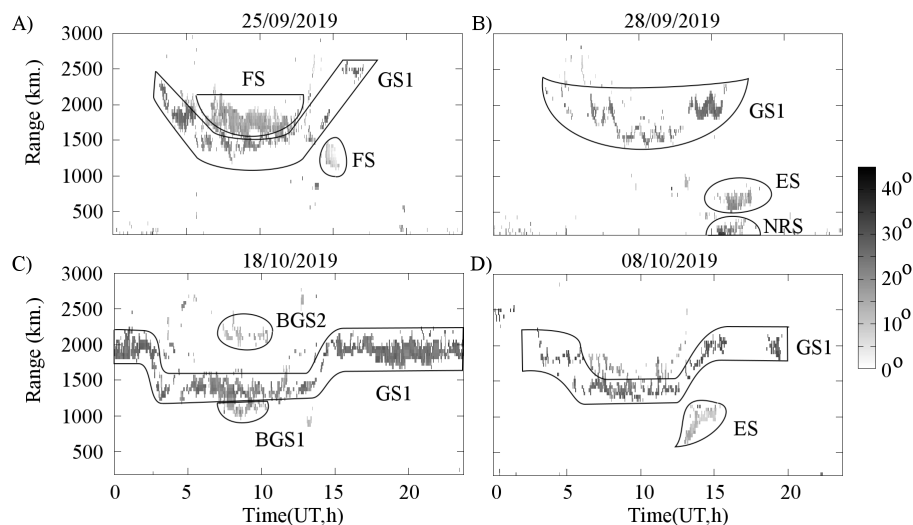


Figure 9: Examples of calculations of elevation angles and approximate identification of signal types in various experiments. GS1 is ground scatter, 1st hop; BGS1 is ground scatter at back lobe, 1st hop; BGS2 is ground scatter at back lobe, 2nd hop; FS is F region ionospheric scatter; ES is E-region ionospheric scatter; NRS is near range scatter.

4. Conclusion

The method for calibrating elevation measurements at EKB ISTP SB RAS radar obtained for the period 20/09/2019 - 18/11/2019 is presented.

The calibration method is a modernization of the method for calibrating radar by meteor trails, proposed in (Chisham and Freeman, 2013; Chisham, 2018). The main difference of the method is the use of not a statistically processed FitACF data, but the full waveform of the signals scattered on the meteor trails. Using the full waveform makes it possible to more reliably distinguish meteor scattering from other possible scattered signal sources, and to determine meteor heights from the trail lifetime using the NRLMSIS-00 model. Due to the complex frequency dependence of the phase difference at the EKB radar, the calibration was performed only for the frequency range 10-12 MHz, used for regular observations. A comparison of the results with the method of (Ponorenko et al., 2018) demonstrated a good agreement.

Based on a statistical analysis of the usability of the technique was demonstrated on the processed FitACF data. It is shown that the obtained elevation data on average corresponds well to the expected elevation angles. It is shown that up to 450 km range, meteor scattering can be considered dominant. The first examples of regular elevation observations at the EKB ISTP SB RAS radar are presented, and their preliminary interpretation is given.

Acknowledgments

EKB ISTP SB RAS facility from Angara Center for Common Use of scientific equipment (<http://ckp-rf.ru/ckp/3056/>) is operated under budgetary funding of Basic Research program II.12. The data of EKB ISTP SB RAS radar are available at ISTP SB RAS (http://sdrus.iszf.irk.ru/ekb/page_example/simple). The work of OB,RF, and KG is supported by RFBR grant 18-05-00539a.

References

- Berngardt, O., Ruohoniemi, J., Nishitani, N., Shepherd, S., Bristow, W., Miller, E., 2018. Attenuation of decameter wavelength sky noise during x-ray solar flares in 2013 - 2017 based on the observations of midlatitude HF radars. *Journal of Atmospheric and Solar-Terrestrial Physics* 173, 1 – 13. doi:<https://doi.org/10.1016/j.jastp.2018.03.022>.
- Berngardt, O.I., Kutelev, K.A., Kurkin, V.I., Grkovich, K.V., Yampolsky, Y.M., Kashcheyev, A.S., Kashcheyev, S.B., Galushko, V.G., Grigorieva, S.A., Kusonsky, O.A., 2015a. Bistatic Sounding of High-Latitude Ionospheric Irregularities Using a Decameter EKB Radar and an UTR-2 Radio Telescope: First Results. *Radiophysics and Quantum Electronics* 58, 390–408. doi:[10.1007/s11141-015-9614-1](https://doi.org/10.1007/s11141-015-9614-1).
- Berngardt, O.I., Zolotukhina, N.A., Oinats, A.V., 2015b. Observations of field-aligned ionospheric irregularities during quiet and disturbed conditions with

- EKB radar: first results. *Earth, Planets and Space* 67, 143. doi:10.1186/s40623-015-0302-3.
- Bland, E.C., McDonald, A.J., de Larquier, S., Devlin, J.C., 2014. Determination of ionospheric parameters in real time using SuperDARN HF Radars. *Journal of Geophysical Research: Space Physics* 119, 5830–5846. doi:10.1002/2014JA020076.
- Burrell, A.G., Yeoman, T.K., Milan, S.E., Lester, M., 2016. Phase calibration of interferometer arrays at high-frequency radars. *Radio Science* 51, 1445–1456. doi:10.1002/2016rs006089.
- Chisham, G., 2018. Calibrating SuperDARN Interferometers Using Meteor Backscatter. *Radio Science* 53, 761–774. doi:10.1029/2017RS006492.
- Chisham, G., Freeman, M., 2013. A reassessment of SuperDARN meteor echoes from the upper mesosphere and lower thermosphere. *Journal of Atmospheric and Solar-Terrestrial Physics* , -doi:10.1016/j.jastp.2013.05.018.
- Chisham, G., Lester, M., Milan, S., Freeman, M., Bristow, W., McWilliams, K., Ruohoniemi, J., Yeoman, T., Dyson, P., Greenwald, R., Kikuchi, T., Pinnock, M., Rash, J., Sato, N., Sofko, G., Villain, J.P., Walker, A., 2007. A decade of the Super Dual Auroral Radar Network (SuperDARN): scientific achievements, new techniques and future directions. *Surveys in Geophysics* , 33–109doi:10.1007/s10712-007-9017-8.
- Gillies, R., Hussey, G., Sofko, G., Ponomarenko, P., McWilliams, K., 2011. Improvement of HF coherent radar line-of-sight velocities by estimating the refractive index in the scattering volume using radar frequency shifting. *Journal of Geophysical Research* 116, 1302.
- Greenwald, R., Baker, K.B., Dudeney, J.R., Pinnock, M., Jones, T., Thomas, E., Villain, J.P., Cerisier, J.C., Senior, C., Hanuise, C., Hunsucker, R.D., Sofko, G., Koehler, J., Nielsen, E., Pellinen, R., Walker, A., Sato, N., Yamagishi, H.,

1995. Darn/Superdarn: A Global View of the Dynamics of High-Latitude Convection. *Space Science Reviews* 71, 761–796. doi:10.1007/BF00751350.
- Greenwood, R., Parkinson, M., Dyson, P., Schulz, E., 2011. Dominant ocean wave direction measurements using the TIGER SuperDARN systems 73, 2379–2385.
- Holdsworth, D.A., Reid, I.M., Cervera, M.A., 2004. Buckland Park all-sky interferometric meteor radar. *Radio Science* 39, 1–12. doi:10.1029/2003rs003014.
- Hosokawa, K., Ogawa, T., Arnold, N.F., Lester, M., Sato, N., Yukimatu, A., 2005. Extraction of polar mesosphere summer echoes from superdarn data. *Geophys. Res. Lett.* 32, L12801. doi:10.1029/2005g1022788.
- Hosokawa, K., Ogawa, T., Yukimatu, A., Sato, N., Iyemori, T., 2004. Statistics of antarctic mesospheric echoes observed with the superdarn syowa radar. *Geophys. Res. Lett.* 31, L02106. doi:10.1029/2003g1018776.
- Jones, W., Jones, J., 1990. Ionic diffusion in meteor trains. *Journal of Atmospheric and Terrestrial Physics* 52, 185–191. doi:10.1016/0021-9169(90)90122-4.
- Koustov, A., Andre, D., Turunen, E., Raito, T., Milan, S., 2007. Heights of SuperDARN F region echoes estimated from the analysis of HF radio wave propagation 25, 1987–1994.
- Lester, M., Chapman, P., Cowley, S., Crooks, S., Davies, J., Hamadyk, P., McWilliams, K., Milan, S., Parsons, M., Payne, D., Thomas, E., Thornhill, J., Wade, N., Yeoman, T., Barnes, R., 2004. Stereo CUTLASS - A new capability for the SuperDARN HF radars 22, 459–473.
- MMANA-GAL software, . MMANA-GAL software. URL: <http://gal-ana.de/basicmm/en/>.
- Nishitani, N., Ruohoniemi, J., Lester, M., Baker, J.B.H., Koustov, A.V., Shepherd, S.G., Chisham, G., Hori, T., Thomas, E.G., Makarevich, R.A., Mar-

- chaudon, A., Ponomarenko, P., Wild, J.A., Milan, S.E., Bristow, W.A., Devlin, J., Miller, E., Greenwald, R.A., Ogawa, T., Kikuchi, T., 2019. Review of the accomplishments of mid-latitude Super Dual Auroral Radar Network (SuperDARN) HF radars. *Progress in Earth and Planetary Science* 6, 27. doi:10.1186/s40645-019-0270-5.
- NRLMSISE-00, . NRLMSISE-00 site. URL: <https://ccmc.gsfc.nasa.gov/pub/modelweb/atmospheric/msis/nrlmsise00/>.
- Ogunjobi, O., Sivakumar, V., Stephenson, J.A.E., Sivla, W.T., 2015. Evidence of Polar Mesosphere Summer Echoes Observed by SuperDARN SANA E HF Radar in Antarctica. *Terrestrial, Atmospheric and Oceanic Sciences* 26, 431. doi:10.3319/tao.2015.03.06.01(aa).
- Picone, J.M., Hedin, A.E., Drob, D.P., Aikin, A.C., 2002. NRLMSISE-00 empirical model of the atmosphere: Statistical comparisons and scientific issues. *Journal of Geophysical Research: Space Physics* 107, SIA 15–1–SIA 15–16. doi:10.1029/2002JA009430.
- Ponomarenko, P., Iserhienrhien, B., St.-Maurice, J.P., 2016. Morphology and possible origins of near-range oblique HF backscatter at high and midlatitudes. *Radio Science* 51, 718–730. doi:10.1002/2016rs006088.
- Ponomarenko, P., Nishitani, N., Oinats, A.V., Tsuya, T., St.-Maurice, J.P., 2015. Application of ground scatter returns for calibration of HF interferometry data. *Earth, Planets and Space* 67, 138. doi:10.1186/s40623-015-0310-3.
- Ponomarenko, P., St.-Maurice, J.P., Hussey, G., Koustov, A., 2010. HF ground scatter from the polar cap: Ionospheric propagation and ground surface effects. *J. Geophys. Res* 115, 10310. doi:10.1029/2010JA015828.
- Ponomarenko, P., St.-Maurice, J.P., McWilliams, K., 2018. Calibrating HF Radar Elevation Angle Measurements Using E Layer Backscatter Echoes. *Radio Science* 53, 1438–1449. doi:10.1029/2018rs006638.

- Ponomarenko, P., St-Maurice, J.P., Waters, C.L., Gillies, R., Koustov, A., 2009. Refractive index effects on the scatter volume location and Doppler velocity estimates of ionospheric HF backscatter echoes. *Ann. Geophys.* 27, 4207–4219. doi:10.5194/angeo-27-4207-2009.
- Ribeiro, A.J., Ruohoniemi, J., Ponomarenko, P., N. Clausen, L.B., Baker, J., Greenwald, R., Oksavik, K., de Larquier, S., 2013. A comparison of SuperDARN ACF fitting methods. *Radio Science* 48, 274–282. doi:10.1002/rds.20031.
- Tsutsumi, M., Holdsworth, D., Nakamura, T., Reid, I., 1999. Meteor observations with an mf radar. *Earth, Planets and Space* 51, 691–699. URL: <https://doi.org/10.1186/BF03353227>, doi:10.1186/BF03353227.
- Tsutsumi, M., Yukimatu, A., Holdsworth, D.A., Lester, M., 2009. Advanced SuperDARN meteor wind observations based on raw time series analysis technique. *Radio Sci.* 44, RS2006. doi:10.1029/2008rs003994.
- Villain, J.P., Greenwald, R.A., Vickrey, J.F., 1984. HF ray tracing at high latitudes using measured meridional electron density distributions. *Radio Science* 19, 359–374. URL: <https://agupubs.onlinelibrary.wiley.com/doi/abs/10.1029/RS019i001p00359>, doi:10.1029/RS019i001p00359.
- Yukimatu, A.S., Tsutsumi, M., 2002. A new SuperDARN meteor wind measurement: Raw time series analysis method and its application to mesopause region dynamics. *Geophysical Research Letters* 29, 42–1–42–4. doi:10.1029/2002GL015210.